LETTER Communicated by Jack Cowan

Neural Field Model of Receptive Field Restructuring in Primary Visual Cortex

Katrin Suder
Florentin Wörgötter
Institute of Physiology, Department of Neurophysiology, Ruhr-University, D-44780 Bochum, Germany

Thomas Wennekers
Max-Planck-Institute for Mathematics in the Sciences, D-04103 Leipzig, Germany

Receptive fields (RF) in the visual cortex can change their size depending on the state of the individual. This reflects a changing visual resolution according to different demands on information processing during drowsiness. So far, however, the possible mechanisms that underlie these size changes have not been tested rigorously. Only qualitatively has it been suggested that state-dependent lateral geniculate nucleus (LGN) firing patterns (burst versus tonic firing) are mainly responsible for the observed cortical receptive field restructuring. Here, we employ a neural field approach to describe the changes of cortical RF properties analytically. Expressions to describe the spatiotemporal receptive fields are given for pure feedforward networks. The model predicts that visual latencies increase nonlinearly with the distance of the stimulus location from the RF center. RF restructuring effects are faithfully reproduced. Despite the changing RF sizes, the model demonstrates that the width of the spatial membrane potential profile (as measured by the variance σ of a gaussian) remains constant in cortex. In contrast, it is shown for recurrent networks that both the RF width and the width of the membrane potential profile generically depend on time and can even increase if lateral cortical excitatory connections extend further than fibers from LGN to cortex. In order to differentiate between a feedforward and a recurrent mechanism causing the experimental RF changes, we fitted the data to the analytically derived point-spread functions. Results of the fits provide estimates for model parameters consistent with the literature data and support the hypothesis that the observed RF sharpening is indeed mainly driven by input from LGN, not by recurrent intracortical connections.

1 Introduction

Receptive fields (RFs), defined as the retinal area where a stimulation of receptors causes a recorded neuron to respond, play a key role in identi-

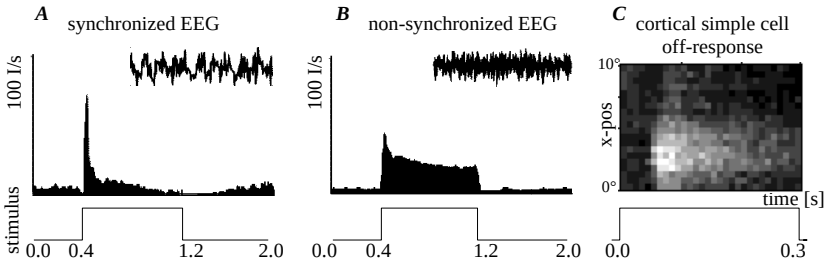

Figure 1: (A,B) Peristimulus-time histograms of an LGN relay cell during different EEG states in an anesthetized cat. Insets show EEG traces (5 s). (C) Shrinking of RF width of a cortical cell during a nonsynchronized EEG state. The cell starts firing roughly 50 ms after stimulus onset. The RF covers approximately 6 degrees at maximum and drops to less than 4 degrees afterward. Firing rates are gray-scale coded (0-40 I/s).

fying the functional mechanisms of visual neural circuits (Hubel & Wiesel, 1962; Levine & Shefner, 1991). For a long time, RFs have been envisaged as pure spatial phenomena with temporally fixed properties. In recent years, though, sophisticated reverse correlation techniques have been developed to study spatial and temporal properties of RFs (DeAngelis, Ohzawa, & Freeman, 1993, 1995; Eckhorn, Krause, & Nelson, 1993). Elaborated physiological experiments now support the viewpoint that RFs are highly dynamic entities that can change due to cortex-intrinsic dynamical processes, context effects, attention, or synaptic plasticity (DeAngelis et al., 1993; Eckhorn et al., 1993; Gilbert, 1998; Shevelev, Volgulshev, & Sharaev, 1992).

Recently, Wörgötter et al. (1998) demonstrated that spatial and temporal characteristics of RFs can, in addition, be modulated by the global state of the brain as, for instance, characterized by the electroencephalogram (EEG). It has been shown that cortical RFs in V1 are wider during synchronized EEG (dominated by α- and δ-waves) than during less or nonsynchronized β-EEG. Moreover, the RF width can shrink considerably over time in response to a flashed stimulus in nonsynchronized states (see Figure 1C and Wörgötter et al., 1998).

It is believed that α- and δ-waves are more common during drowsiness and weak sleep and that less synchronized fast rhythms are associated with alert states. Therefore, the experimental results suggest that information processing is adapted to different behavioral states by qualitative RF changes and that the spatial resolution of visual processing is particularly high in alert states.

Different firing patterns of cells in the lateral geniculate nucleus (LGN) during the different EEG states have been suggested as the main mechanism for this restructuring. Figure 1A shows that during synchronized EEG, a

strong contrast independent burst component dominates the response to a flashed light spot. After that, only a small, persistent response remains, although the stimulus is still on. In contrast, during nonsynchronized EEG, LGN cells respond with a long-lasting tonic firing pattern at intermediate (contrast dependent) rates, whereas the burst component is often diminished (see Figure 1B).

Wörgötter et al. (1998) hypothesized that these state-dependent LGN firing patterns essentially drive the cortical field changes. Basically, it is assumed that the LGN cells excited by the flash stimulus innervate a local region in the visual cortex with decreasing (e.g., gaussian) effective strength from the projection center. Taking firing thresholds of cortical cells into account, it is then obvious that higher LGN firing rates are able to elicit spikes in a larger part of the cortical projection region than lower rates. Accordingly, the cortical point spread function—and the cortical RF, respectively—will be broad during the initial burst component and will sharpen afterward, when LGN firing rates decline. During synchronized EEG, the late cortical response component can also be missing if LGN cells fire too seldom to raise cortical cells above threshold at all.

We tested this hypothesis in a detailed biophysical model of the visual pathway (Wörgötter et al., 1998) comprising regular firing cells in area V1, two-state neurons in the LGN (burst and regular firing mode), and a modulatory influence of the perigeniculate nucleus (PGN), which is supposed to be involved in the control of the different excitability of LGN cells during drowsy and alert states (Ahlsén & Lo, 1982; Funke & Eysel, 1998; McCormick, 1992). Although in this model particularly lateral connections in V1 and feedback from V1 to LGN were considered, the simulations indicated that the experimentally observed cortical state dependencies are mainly due to a feedforward effect; feedback has only a weak modulatory influence on late-response components or destabilizes the network if it is too strong (see Wörgötter et al., 1998; Crick & Koch, 1998). In principle, the recurrent loop between V1 and LGN can broaden RFs in V1 further. However, this is in contrast to our experimental findings. Thus, recurrent connections do not seem to contribute significantly to the RF size effects described above.

The relative influence of afferent versus cortex-intrinsic signals to orientation tuning of cortical simple cells has been studied previously by several authors in experiments (Ferster, Chung, & Wheat, 1996; Henry, Michalski, Wimbourne, & McCart, 1994; Sato, Katsuyama, Tamura, Hata, & Tsumoto, 1996) as well as in simulations (Adorjan, Levitt, Lund, & Obermayer, 1999; Ben-Yishai, Bar-Or, & Sompolinsky, 1995; Carandini & Ringach, 1997; Somers, Nelson, & Sur, 1995). It still remains controversial whether orientation tuning arises from already sharply tuned input to cortical cells, as originally suggested by Hubel and Wiesel (1962) or whether LGN input is only weakly tuned but amplified and sharpened by recurrent excitatory and inhibitory connections. Experimental evidence for both viewpoints ex-

ists (reviews in Sompolinsky & Shapley, 1997; Vidyasagar, Pei, & Vogulshev, 1996).

In contrast, our experimental data and detailed simulations indicate evidence for some purely input-driven RF properties. To validate their feedforward nature more thoroughly, a phenomenological neural field model of the LGN-V1-projection is developed in this article (section 2). The advantage of this model as compared to biologically detailed ones is that it can be solved exactly. This way, explicit equations for cortical point-spread functions, latencies, and RF-width profiles become available (section 3). They can be compared with simulated profiles appearing in recurrent models (section 4) and, most important, can be fitted to the experimental data (section 5). The results of the fit in comparison with the two different model approaches (feedforward versus feedback) validate the feedforward ansatz.

2 Feedforward Neural Field Model

In this section we develop a neural field approach to study the LGN-V1-projection. The simple structure of the resulting equations allows us to compute cortical response functions analytically for input-driven activity in V1. Neural fields have been used for similar purposes, although usually in simulation studies (Giese, 1999; Krone, Mallot, Palm, & Schüz, 1986; Mineiro & Zipser, 1998; Sabatini & Solari, 1999; Wilson & Cowan, 1973; Wörgötter, Niebur, & Koch, 1991).

The purpose of this section is to study the input-driven dynamics of V1. Therefore, we consider just one field $V(x, t)$ for V1 and neglect recurrent connections inside it (the latter are included in section 4). For convenience, we further idealize V1 as a one-dimensional field, $x \in \mathbb{R}$, and assume that the activity in the LGN and V1 is spatiotemporally separable, $V(x, t) = X(x)T(t)$ (see DeAngelis et al., 1995; Mineiro & Zipser, 1998)). Including a leakage term, the temporal development of the membrane potential V is given by

$$\tau \frac{dV(x,t)}{dt} = -V(x,t) + \int_{-\infty}^{\infty} K(x-x') I_{syn}(x',t) dx' \,, \tag{2.1}$$

where τ is a phenomenological time constant. The kernel $K(x)$ describes the synaptic feedforward projection from the LGN input I to cortex. We choose a gaussian connectivity profile,

$$K(x) = \frac{K_0}{\sqrt{2\pi}} \, e^{-\frac{x^2}{2\sigma_0^2}} \,, \tag{2.2}$$

with effective synaptic strength $K_0/\sqrt{2\pi}$ and width σ_0. This represents a single on- or off-subfield. Simple cell RFs consisting of several subfields can be represented by superposition of responses of the form equation 2.1 with appropriate kernels.

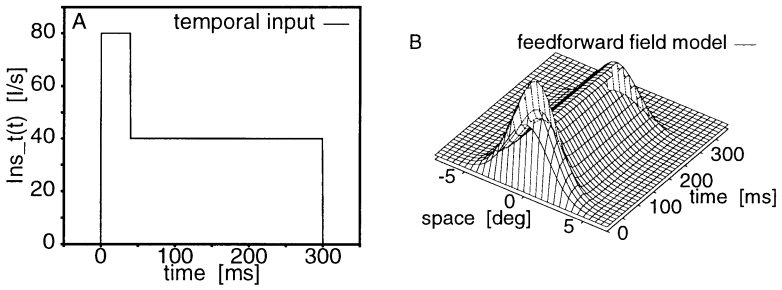

Figure 2: (A) Temporal input function $Ins_t(t)$ used to simulate LGN firing during nonsynchronized EEG. Observe the two idealized components representing the burst and tonic phase (see equation 2.5). (B) Simulation of the cortical membrane potential $V(x, t)$ in the nonsynchronized state. Simulation parameters are $\sigma_0 = 1.7^\circ$, $\sigma_1 = 0.5^\circ$, $\tau = 10.0\,ms$, $t_0 = 0\,ms$, $t_1 = 40\,ms$, $t_2 = 300\,ms$, $c_1 = 80\,I/s$, $c_2 = 40\,I/s$.

The synaptic input currents I_{syn} in V1 are fully described by the activity of the LGN cells $I(x, t)$, which is gaussian in space and square wave in time (see below). Detailed dynamical processes in the LGN are not explicitly modeled but considered in the form of phenomenological spatiotemporally separable input functions $I(x, t) = I_x(x)I_t(t)$. According to the experimental input in the form of small, light spots, the spatial input I_x has a gaussian shape in our model, which represents a localized activity profile in the LGN. The temporal input component I_t contains the EEG-state dependence and approximates the experimentally observed temporal firing patterns of LGN cells (see Figures 1A and 1B):

$$I_x(x) = e^{-\frac{x^2}{2\sigma_1^2}} \tag{2.3}$$

$$Is_t(t) = c_1\Theta(t - t_0)\Theta(t_1 - t) \tag{2.4}$$

$$Ins_t(t) = Is_t(t) + c_2\Theta(t - t_1)\Theta(t_2 - t). \tag{2.5}$$

Here, $\Theta(t)$ is the Heaviside function. The function $Is_t(t)$ describes the high-frequency burst of spikes in the synchronized EEG in the form of a rectangular pulse of strength c_1 lasting from $t = t_0$ to t_1. $Ins_t(t)$ describes the nonsynchronized case and contains, in addition, a tonic component of height c_2 ($< c_1$) lasting from t_1 to t_2 (see Figure 2A).

Firing rates R are derived from the membrane potential V by means of a rectifying function,

$$R = [\beta V - \vartheta]_+, \tag{2.6}$$

where β is the neuronal gain (in spikes/mV/s) and ϑ the firing threshold. The function $[x]_+$ is zero for $x \leq 0$ and equal to x above zero.

Figure 2B shows a simulation of the model. The cortical membrane potential V is plotted as a function of space and time for the nonsynchronized state. In accordance with the experimental data (see Figure 1C) a phasic peak is followed by a tonic component with a reduced amplitude. Furthermore, a restructuring of the potential takes place between 50 and 70 ms.

3 Response Function and Equipotential Lines

We now derive analytical expressions for the cortical membrane response. Because we assume stimulation by small, light spots, $V(x, t)$ can be interpreted as the cortical point-spread function or, in the light of the linearity of the membrane and the spatial homogeneity of the model, as the spatiotemporal RF of the model cells. Inserting the assumptions 2.2 and 2.3–2.5 into equation 2.1 and integrating, one obtains the spatial and temporal components $X(x)$ and $T(t)$. Thereby, we set $V(x, t_0) = 0$, which means that potentials are measured relative to a resting potential of zero. $X(x)$ is a convolution of two gaussians: the input distribution $I_x(x)$ and the feedforward kernel $K(x)$. Thus,

$$X(x) = \frac{K_0\sigma_0\sigma_1}{\sqrt{\sigma_0^2+\sigma_1^2}}\, e^{-\frac{x^2}{2(\sigma_0^2+\sigma_1^2)}} = \frac{K_0\sigma_0\sigma_1}{\sigma_r}\, e^{-\frac{x^2}{2\sigma_r^2}} \approx K_0\sigma_1\, e^{-\frac{x^2}{2\sigma_0^2}}, \tag{3.1}$$

where $\sigma_r^2 := \sigma_0^2 + \sigma_1^2$ is the resulting width of the cortical membrane potential. The approximation holds for small stimuli, $\sigma_1 \ll \sigma_0$, that is, for point stimulation. Within this limit, larger stimuli, σ_1, increase potential values approximately linearly, but the width of the cortical response is determined only by the width of the projection from LGN to cortex, σ_0.

The temporal amplitude factor $T(t)$ represents the response of a low-pass filter to the input $I_t(t)$. In the nonsynchronized state, $I_t(t) = Ins_t(t)$, one gets

$$T(t) = \begin{cases} 0 & : \quad t < t_0 \\ c_1(1 - e^{-\frac{t-t_0}{\tau}}) & : \quad t_0 \le t < t_1 \\ c_2 - c_1 e^{-\frac{t-t_0}{\tau}} + (c_1 - c_2)e^{-\frac{t-t_1}{\tau}} & : \quad t_1 \le t < t_2 \\ c_2 e^{-\frac{t-t_2}{\tau}} - c_1 e^{-\frac{t-t_0}{\tau}} + (c_1 - c_2)e^{-\frac{t-t_1}{\tau}} & : \quad t_2 \le t. \end{cases} \tag{3.2}$$

The synchronized response $T(t)$ is obtained from equation 3.2 by setting the tonic component to zero, that is, $c_2 = 0$. The time course of T is determined by the height (c_1) and duration ($t_0 - t_1$) of the burst and the tonic component (c_2, $t_1 - t_2$), and by the time constant τ.

Until now, potentials and not firing rates, as typically observed in experimental recordings, were considered. To obtain rates from the membrane potential, a threshold function has to be introduced (cf. equation 2.6). A useful concept in this context are lines of equal potential defined by

$$V(x, t) = X(x)T(t) = \kappa = constant. \tag{3.3}$$

Relation 3.3 can be solved for either $x = x(t;\kappa)$ or $t = t(x;\kappa)$, giving the equipotential lines in parameterized form. Of particular interest is the case where κ equals the firing threshold ϑ of cortical cells (which is assumed to be the same for all cells; the exact form of the output function above threshold does not matter at this point). Then, $w(t) := x(t;\kappa = \vartheta)$ describes the time course of the boundary between silent (subthreshold) and firing (superthreshold) cells. This is equivalent to the width of spatiotemporal RFs as observed experimentally by extracellular recordings of firing rates (see also Figure 3A). Inserting the spatial profile $X(x)$ from equation 3.1 into equation 3.3 and isolating x, we get

$$x^2(t;\kappa) = 2\sigma_r^2 \ln\left[\frac{K_0\sigma_0\sigma_1}{\kappa\sigma_r}T(t)\right] \overset{\sigma_1 \ll \sigma_0}{\approx} 2\sigma_0^2 \ln\left[\frac{K_0\sigma_1}{\kappa}T(t)\right]. \tag{3.4}$$

The time dependence enters into equation 3.4 via the amplitude function $T(t)$. Using equation 3.2 for $T(t)$, we obtain the RF width for flashed stimuli. Examples, shown in Figure 3B, reveal that the width of the (superthreshold) RF, $w(t)$, indeed changes with time as in the experiments, although the width σ_r of the (subthreshold) potential profile is constant (see equation 3.1). The reason for this difference is that the spatial profile $X(x)$ is simply modulated by the multiplicative amplitude function $T(t)$. Then, as long as the firing threshold of cortical cells, ϑ, is constant, the width of the region of cells above threshold naturally varies, but the width of $X(x)$, of course, does not (see Figure 3A). $w(t) = x(t;\kappa)$ from equation 3.4 predicts the time course of the RF modulation.

Equation 3.4 gives a predictable dependence of the RF boundary on the stimulus size, σ_1, which could be tested experimentally. On the other hand, variation of K_0, κ or σ_0 is certainly more complicated, if possible at all. The amplitude function, $T(t)$, however, could be systematically modified by the temporal input $I_t(t)$. This may yield further information about network parameters.

Solving equation 3.3 for $t(x)$, we get the times when the cortical cells cross a threshold level κ:

$$t(x;\kappa) = \begin{cases} t_0 - \tau \ln\left(1 - \frac{\kappa}{c_1 X(x)}\right) & : \quad t_0 < t \le t_1 \\ \vdots & \vdots \\ -\tau \ln\left(\frac{\frac{\kappa}{X(x)} - c_2}{-c_1 e^{\frac{t_0}{\tau}} + (c_1 - c_2)e^{\frac{t_1}{\tau}}}\right) & : \quad t_1 < t \le t_2 \\ \vdots & \vdots \\ -\tau \ln\left(\frac{\kappa}{X(x)(c_2 e^{\frac{t_2}{\tau}} - c_1 e^{\frac{t_0}{\tau}} + (c_1 - c_2)e^{\frac{t_1}{\tau}})}\right) & : \quad t_2 < t. \end{cases} \tag{3.5}$$

Times $t(x;\kappa)$ in the range $t_0 < t \le t_1$ describe cortical latencies (i.e., the threshold is crossed from below), times in the range $t_1 < t \le t_2$ are off-times due to decreasing potentials when the LGN firing rates switch from high (c_1, bursts) to low (c_2, tonic firing), and the last regime, $t_2 < t$, characterizes

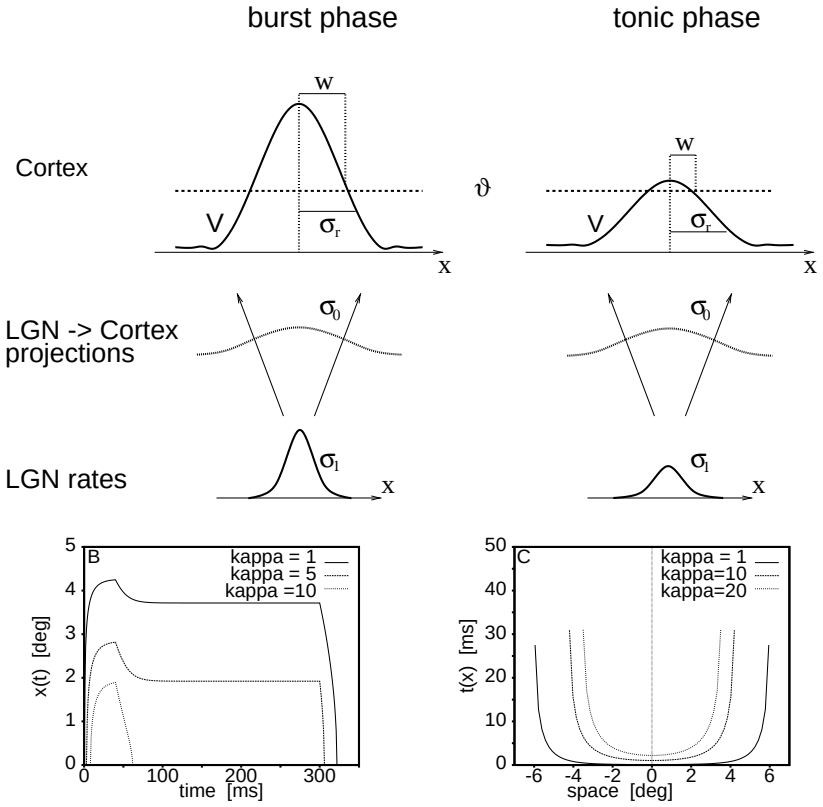

Figure 3: (A) Illustration of the mechanism leading to a sharpening of the RF. The width of the cortical membrane potential, σ_r, is the same during the burst and tonic phase, but the width of the firing-rate profile w varies due to the LGN-driven amplitude modulation of the region of cells above threshold, ϑ. (B, C) Simulation of equipotential lines $x(t, \kappa)$ and $t(x, \kappa)$ for different threshold levels κ. For $\kappa = \vartheta$ such borders between subthreshold and superthreshold cells define the dynamic RF width $w(t) = x(t; \kappa = \vartheta)$ and the firing latencies $t(x, \vartheta)$. Note that $x(t, \kappa)$ shrinks with the transition from burst to tonic phase around 50 ms. Simulation parameters are the same as for Figure 2.

off-times when the LGN activity is over. Some curves for cortical latencies are depicted in Figure 3C. Inserting equation 3.1 for the spatial profile $X(x)$, a useful approximation for these cortical onset times can be given:

$$t(x) - t_0 \approx \frac{\kappa\tau}{c_1 X(x)} \approx \frac{\kappa\tau}{K_0 c_1 \sigma_1}\left(1 + \frac{x^2}{2\sigma_0^2}\right) . \tag{3.6}$$

This means that as long as $x \ll \sigma_0$, the latencies increase quadratically with distance x. A correlation between firing times and distance from RF center has indeed been observed, but the details of its dependence are still under examination (Bringuier, Chavane, Glaeser, & Frégnac, 1999; Celebrini, Thorpe, Trotter, & Imbert, 1993; Dinse & Krüger, 1994; Ikeda & Wright, 1975; Wörgötter, Opara, Funke, & Eysel, 1996). Equation 3.6 further shows that the latencies are shorter for stronger cortical inputs ($K_0 c_1$) or larger stimuli (σ_1), and that they increase with firing thresholds, or with membrane time constant τ, respectively.

4 Recurrent Neural Field Model

In this section we qualitatively explore the influence of recurrent intracortical connections on the cortical potential by adding a feedback loop to the simple feedforward model:

$$\tau \frac{\partial V(x,t)}{\partial t} = -V(x,t) + X(x) I_t(t) + \int_{-\infty}^{\infty} K_{DOG}(x - x') R(V(x',t))\, dx'. \tag{4.1}$$

The cortical connection kernel K_{DOG} is chosen as a difference of gaussians to include excitatory and inhibitory feedback:

$$K_{DOG}(x) = \frac{K_{exc}}{\sqrt{2\pi}} e^{-\frac{x^2}{2\sigma_{exc}^2}} - \frac{K_{inh}}{\sqrt{2\pi}} e^{-\frac{x^2}{2\sigma_{inh}^2}}. \tag{4.2}$$

Parameters are such that K_{DOG} has a Mexican hat profile (see below). The rate function $R(V)$ in equation 4.1 is zero for $V \leq 0$ and equal to βV for $V > 0$ (cf. equation 1.6). β is the neuronal gain (in spikes/s/mV). Input from LGN is the same as in the feedforward model. Note, however, that in equation 4.1, we have already inserted the total spatial input $X(x)$ into cortex, that is, the spatial convolution of the LGN activity $I_x(x)$, equation 1.3, and the feedforward kernel, equation 1.2, from LGN to cortex. The temporal input component I_t in equation 4.1 is again given by equation 1.5. Similar models have been investigated recently in the context of orientation tuning in V1 (Adorjan et al., 1999; Ben-Yishai et al., 1995; Carandini & Ringach, 1997).

Due to the nonlinearity, analytical solutions of equation 4.1 cannot be given. Therefore, we simulate equation 4.1 and discuss the qualitative differences that appear in contrast to the simple feedforward model. As parameters, we choose $\tau = 10$ ms, $t_0 = 0$ ms, $t_1 = 50$ ms, $t_2 = 300$ ms and (somewhat arbitrarily) $\sigma_r = 3^\circ$, $\sigma_{exc} = 0.7^\circ$, $\sigma_{inh} = 3.0^\circ$, $K_{exc}\beta = 2.0\,\mathrm{mV/deg}$, and $K_{inh}\beta = 0.5\,\mathrm{mV/deg}$. Furthermore, we define $k := K_0 \sigma_0 \sigma_1 / \sigma_r$, $C_1 = k c_1$, $C_2 = k c_2$ and choose the effective cortical inputs $C_1 = 10$ mV and $C_2 = 2.5$ mV for the burst and the tonic phase. With these parameters, the network operates in a regime of cortical amplification, as it has been proposed for

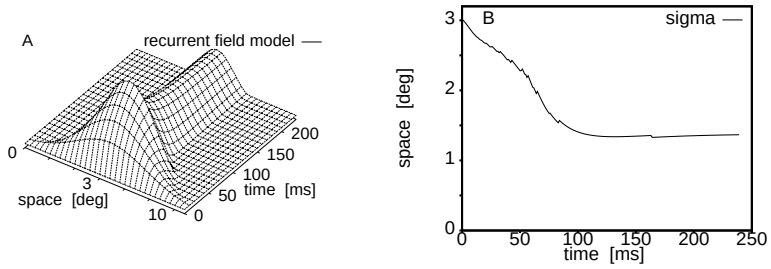

Figure 4: (A) Simulation of the recurrent neural field model. (B) Time course of the width of the potential $V(x, t)$ for the data shown in A.

recurrent orientation tuning models (Adorjan et al., 1999; Ben-Yishi et al., 1995; Carandini & Ringach, 1997; Somers et al., 1995).

Figure 4A shows that the simulated membrane potential looks quite similar to the response of the simple feedforward model (see Figure 2B) and also to the experimental data (see Figure 1C). Again, a strong and wide component dominates during the first 50 ms and is followed by a weaker and smaller tonic component. This behavior is typical for large parameter regimes as long as the cortical gain is not too high, recurrent net excitation and inhibition are of roughly the same order, and LGN firing rates in the burst phase are significantly larger than in the tonic phase.

Although at first glance the potential $V(x, t)$ looks similar in the feedforward and the recurrent models, there is nonetheless a subtle but important difference. This becomes visible if we look at the width of the simulated potential profile. As emphasized earlier, the width is constant in time and equal to σ_r in the feedforward model. Strictly speaking, the width is not well defined in the recurrent model, because the potential profile is no longer gaussian. We can, however, fit the central peak of the profile to a gaussian function to obtain an effective width, $\sigma(t)$. Figure 4B shows $\sigma(t)$ obtained this way for the data in Figure 4A. Obviously the width now depends on time, in strong contrast to the feedforward case.

These temporal changes are, of course, due to the feedback connections. At any instance of time, the potential can be roughly envisaged as a superposition of components resulting from the LGN input and the excitatory as well as the inhibitory feedback. The relative contribution of these components changes with time. Initially, cortical cells are silent. Accordingly, the feedback is zero, and only the input determines the width of the potential distribution at the very early response. Thus, $\sigma(t = 0) = \sigma_r$. As the firing activity rises, the width σ declines, because the excitatory recurrent connections are relatively strong and sharply tuned ($\sigma_{exc} = 0.7$ degree), while input and inhibition are not ($\sigma_r = \sigma_{inh} = 3.0$ degrees). This way, the intracortical amplification leads to a gradual change from wide to sharply tuned spatial profiles.

The parameter dependence of the time course of σ is complex and cannot be given in a closed form. It is important that a time dependence occurs generically in feedback models for almost all parameter values. This is true whether the model is built of two mutually connected fields that represent excitatory and inhibitory cortical cells separately or of just a single layer like the feedback model in equation 4.1. The time dependence does not have to be in the form of a shrinkage of the width; it is also possible to obtain an increasing $\sigma(t)$ if σ_{exc} is considerably larger than σ_r and σ_{inh}. Anatomical results, however, indicate that the Mexican hat profile with $\sigma_{inh} > \sigma_{exc}$ is the biologically most realistic one (Salin & Bullier, 1995). In that case a time-varying width must appear in feedback models in response to flashed stimuli. This means that a constant width of the potentials, as found in the feedforward model, can be expected only for very special, unrealistic, and nongeneric conditions in a feedback model. Therefore, a constant $\sigma(t)$ in the experimental data would be a strong indicator for a pure feedforward mechanism of the observed RF restructuring.

5 Fit to Experimental Data

We now fit the feedforward model to the experimental data to test whether it can accurately describe the data and to estimate the model parameters. Firing rates $\nu(x, t)$ of on- and corresponding off-subfields of 16 V1 cells recorded during both states of the EEG were analyzed. Each field was sampled at 20 positions with 0.5 degree resolution and for 30 time slices of 10 ms bin size.

For the fit, the potentials $V(x, t)$ are supposed to transform into firing rates R by means of a rectilinear function according to equation 2.6: $R = f(V) = [\beta V - \vartheta]_+ + b$, where b accounts for spontaneous background firing. Then the experimentally derived firing-rate data can be fitted to obtain parameters of the underlying potential distribution. Note, however, that the analytical solution for the potential $V(x, t)$ contains products of model parameters (see equations 3.1 and 3.2). This implies that we cannot determine all model parameters independently. We proceed in two steps: for every time slice t_i, we first determine the parameters of the spatial profile $X(x)$ by nonlinear least-square fits:

$$\nu(x, t_i) \stackrel{fit}{=} \left[q(t_i) e^{-\frac{(x-a)^2}{2\sigma_r^2}} - \vartheta \right]_+ + b, \quad i = 1, 2, \ldots, 30. \tag{5.1}$$

Here, a is an (arbitrary) offset of the RF center, and the $q(t_i)$ are treated as fit parameters. They are proportional to the amplitude factor $T(t_i)$, that is, $q(t_i) = K_0 \sigma_0 \sigma_1 \beta / \sigma_r \cdot T(t_i)$. Therefore, they can be fitted in a second step to the function $T(t)$ (see equation 3.2) to obtain the temporal model parameters. In addition, the procedure provides a sequence of fitted widths $\sigma_r(t_i)$, $i = 1, 2, \ldots$, which can be checked for constancy. All fits are performed using the

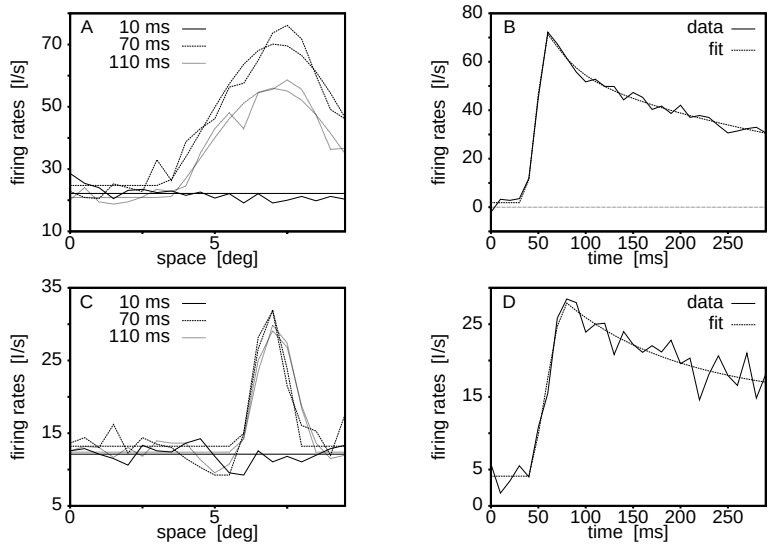

Figure 5: (A) Original data and fit of a cortical simple cell (on-field) to the spatial activity $q(t_i)X(x)$ for selected time slices t_i recorded during nonsynchronized EEG. (B) Temporal fit, $q(t)$. (C, D) Spatial and temporal fit for another example (off-field during nonsynchronized EEG). In *A* and *C*, the fits correspond to the smooth curves.

Levenberg-Marquardt algorithm (Press, Teukolsky, Vetterling, & Flannery, 1993).

On the left side of Figure 5 spatial fits are shown for different time steps of an on-response; the right part shows the temporal fit of $q(t)$. Observe that the LGN activity does not reach V1 before $t_0 \geq 30$ ms. Before that, background noise is fitted. Thus, the resulting fit parameters are meaningless for $t < t_0$. The latency t_0 varies between 30 and 60 ms for different subfields (cf. Figure 5B versus 5D). Off-subfields exhibit a longer delay than on-subfields (Schiller, 1992). Apparently the experimental data can be described very well by the simple feedforward model, although the cells differ significantly in their spatiotemporal receptive field profiles (see Figure 5, top versus bottom). Some of the measured cells were too noisy, though. The data of two off-fields during nonsynchronized EEG and of two on- and four off-fields during synchronized EEG had to be excluded because no receptive field was detectable. In the following, only the remaining 24 subfields were analyzed.

To quantify the quality of the fit, we determined the percentage of fluctuations in the data that remained after the model fit; we calculated

$$P = \frac{1}{N-1} \sum_{i=1}^{N} \frac{(f(x_i) - y(x_i))^2}{y(x_i)^2}, \tag{5.2}$$

separately, for the fit in space and in time. Averaged over all 720 spatial fits (each of the 24 subfields was sampled at 30 different time steps) we determined that $P = 0.092 \pm 0.059$, which means that only 10% of the variation in the data cannot be explained by the fit.

P is of the same magnitude as the noise contained in the data. The latter can be quantified by the standard deviation of the background activity (roughly 10%) during the first 30 ms of the response, where the LGN firing does not yet influence cortical firing. Comparability of both measures—background noise and fit error—implies that the model consistently describes the deterministic variation in the data (Press et al., 1993).

Comparing the fit for the two EEG states, it was slightly better for the nonsynchronized state ($P = 0.083$ compared to $P = 0.100$). The temporal fit is as good as the spatial. Averaged over all 24 fits, we find $P = 0.107 \pm 0.144$. Again, the fit during synchronized EEG ($P = 0.151$) was not as good as the one during nonsynchronized EEG ($P = 0.063$). In general, the data are noisier in the synchronized EEG than in the nonsynchronized EEG. A major reason for this is probably that twice as many stimulus repetitions were recorded during nonsynchronized than during synchronized EEG.

Interestingly, it turns out that the parameters $\sigma_r(t_i)$, $a(t_i)$, $\vartheta(t_i)$, $b(t_i)$ are almost constant over time after the LGN activity has reached the cortical layer (see Figure 6). To quantify their temporal variation, we calculated standard deviations over all time bins t_i and took the mean over all sampled subfields. Values found are a: 5%, σ_r: 20%, b: 18%, and ϑ: 16%.

The most important result of the fit is shown in Figures 6B–6D, where σ_r, the width of the cortical membrane potential, is plotted as a function of time. After the activity has reached V1 (around $t_0 = 40$ ms in B), σ_r turns out to be constant over time. This was the case in almost all sampled subfields. Only two subfields revealed slight and insignificant trends toward larger values with increasing time. As outlined in section 4, this strongly supports the hypothesis that the RF restructuring is mainly input driven.

RFs in experiments are most commonly derived from firing rates, not intracellular potentials. As a measure for the width of the firing-rate distribution, we can choose its half-width at baseline, w. This can be compared to the width σ_r of the (subthreshold) membrane potential (see Figure 6B), and it is computable from the fitted model parameters using equation 3.4 with $\kappa = \vartheta$, that is, $w^2(t_i) := x^2(t_i; \vartheta_i) = 2\sigma_r^2(t_i) \ln[q(t_i)/\vartheta(t_i)]$. Clearly, w depends on the EEG state, and it is also time dependent although σ_r is not (see Figure 6B). Table 1 shows mean values for σ_r (averaged over all time bins and subfields), as well as maximal field widths w_p and mean values for $w_s := w(200\text{ ms})$ during the late response component. Values for w_p and w_s are averaged over all sampled subfields. w_s roughly corresponds to the half-width of "classical" RF sizes.

Both measures, w and σ_r, and their relation are in agreement with literature data: RFs are consistently smaller when obtained from extracellular rates (compare, e.g., Alonso & Reid, 1995). Hirsch and colleagues mapped

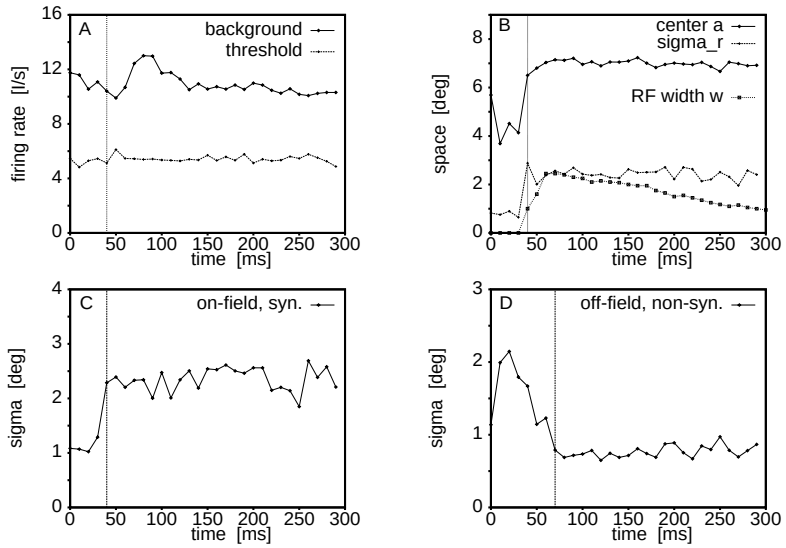

Figure 6: (A, B) Time course of five model parameters for the fit to an on-field of a simple cell during the nonsynchronized state. (A) Background activity b and firing threshold ϑ. (B) Offset a of the center of the gaussian $X(x)$, width of the spatial membrane profile σ_r and half-width of the extracellular firing rate profile w. Note that the LGN activity does not reach V1 before approximately 40 ms (vertical line in A to D); up to that time background noise is fitted. (C, D) Time course of σ_r for two other examples. (C) Same on-subfield as in A and B but during synchronized EEG. σ_r shows a similar time course as for the nonsynchronized EEG but it is noisier. (D) Off-subfield during nonsynchronized EEG also showing a constant σ_r. In C and D the vertical lines again indicate the latency of the onset response, which is larger for the off-subfield in D.

Table 1: State and Time Dependence of RF Widths.

	Intracellular Potential, σ_r	**Extracellular Rates**	
		Peak Width, w_p	Width at $t_i = 200$ ms, w_s
Synchronized	2.2°	2.0°	1.0°
Nonsynchronized	1.8°	1.75°	1.25°

Notes: Intracellular widths, σ_r, measured from membrane potentials are consistently larger than classical RFs determined from firing rates (w_s) and also as the maximal extracellular peak responses w_p of $w(t)$. During synchronized EEG, the classical RF shrinks roughly 50% on average, and somewhat less during the nonsynchronized EEG.

RFs from intracellularly recorded potentials of striate cortical simple cells (Hirsch, Alonso, Reid, & Martinez, 1998). They found fields with diameters up to 4 degrees, consistent with a $\sigma_r \sim 2$ degrees from our data. Intracellular RFs of this size are also compatible with anatomical data (Antonini, Gillespie, Crair, & Stryker, 1998; Chapman, Zahs, & Stryker, 1991; Humphrey, Sur, Uhlrich, & Sherman, 1985).

In a second step, we fitted $q(t_i), i = 1, 2, \ldots, 30$ (see equation 5.1) to $k\beta \cdot T(t)$ with $k := K_0\sigma_0\sigma_1/\sigma_r$ to determine the parameters $\tilde{C}_1 := k\beta c_1$, $\tilde{C}_2 := k\beta c_2$, t_0, t_1, t_2, and τ. Note that only products $k\beta c_i, i = 1, 2$ can be obtained from the fit. t_0 accounts for latencies between stimulus onset and cortical response and $t_1 - t_0$ for the duration of the phasic burst component. t_2 was fixed at 300 ms because data were sampled only during stimulus presentation. For most subfields, excellent fits were obtained (see Figure 5). Some on-subfields in the nonsynchronized case exhibited a significant adaptation during the tonic phase (e.g., Figure 1B, 100–300 ms). In these cases, an adaptation term was added in the fit function, that is, c_2 was replaced by $c_2 \exp(-(t - t_1)/\tau_a)$.

A comparison of the fitted parameters for both EEG states and for on- and off-subfields of the same neuron reveals only a few systematic relations. The main difference between on- and off-subfields is a delayed response for the off-fields of approximately 20 ms ($t_0 = 56$ ms) compared to the on-fields ($t_0 = 35$ ms), which is in accordance with the literature (Schiller, 1992). The main EEG state dependence turns out to be the difference between $\tilde{C}_1$ and $\tilde{C}_2$, which is proportional to the difference between LGN activity during the burst and tonic phase. The difference is about three times as high in the synchronized (29 I/s) as in the nonsynchronized state (9 I/s). Moreover, we find that bursts are more pronounced (40 ± 8 versus 23 ± 6 I/s) and that the tonic component is slightly smaller (11 ± 5 versus 14 ± 7 I/s) during synchronized EEG. This may account for the somewhat larger average peak width (w_p) and the lower stationary width (w_s) in the synchronized state, as revealed by Table 1. Individual cells can show this trend much more clearly than the mean values given in the table. Only in one out of all cells were bursts less pronounced during the synchronized EEG. The tonic component was almost completely missing in about one-third of the cells during synchronized EEG.

The other model parameters do not exhibit dependences on EEG state or subfield type. Especially the parameters of the spatial gaussian profile, a and σ_r, do not show a significant variation. Interestingly, the threshold ϑ also seems to be constant, not only over time but also for different states and RF types of the same cell. Somewhat surprisingly, even the empirical time constant τ shows no significant dependence on the EEG state. Since neuronal membranes tend to have faster response times in depolarized states, one may have expected differences in τ. However, all experiments in Wörgötter et al. (1998) were performed under weak anesthesia, where LGN cells are not as strongly hyperpolarized as in deep sleep. In that range, τ may only weakly

depend on the level of depolarization (Bernander, Douglas, Martin, & Koch, 1991). In addition, synchronized and nonsynchronized states were classified from the spectral content of the EEG during a recording session, that is, the transition between the two states was not induced by other, externally controlled means. Under these conditions, the range of modulation of the resting potentials of LGN cells might have been relatively small, such that τ can be expected to be constant.

Quantitatively analyzing the temporal parameters, we find that they are in agreement with the literature (DeAngelis et al., 1995; Hirsch et al., 1998; Somers et al., 1995; Wörgötter and Koch, 1991): $\tau = 13 \pm 7$ ms, $t_1 - t_0 = 38 \pm 17$ ms, $\tau_a = 320 \pm 50$ ms, and that only the duration of the bursts, $t_1 - t_0$, exhibits a small state dependence: bursts are about 20% longer in the synchronized than in the nonsynchronized EEG.

In addition to the firing rates $\nu(x, t)$ and the RF widths $w(t)$, cortical firing latencies $t_{lat}(x)$ can be analyzed. In particular, it is interesting to see if their spatial distribution is in agreement with the distribution predicted by the model. In the model, $t(x, \kappa)$ describes the equipotential lines of the cortical membrane potential, $V(x, t) = \kappa$, in parameterized form. If the membrane potential equals the firing threshold, $\kappa = \vartheta$, these times are equal to the cortical onset times when the cells start firing, that is, $t_{lat}(x) = t(x, \kappa = \vartheta)$. The model predicts a quadratic dependence $t_{lat} \propto x^2$ of the latencies on the distance x from the RF center as long as x is relatively small in comparison with the projection range of cortical input connections (see equation 3.6). In experiments, these times are measured as firing latencies. They describe the time from the onset of the stimulus to the first response of the recorded cell. As the latencies were not directly recorded in our experiments, cortical onset times were obtained with the following procedure. For each location x, the time step t_i, at which the firing rate first exceeds the background firing rate plus twice the standard deviation of the background firing, was taken as t_{lat}. The binning was changed from 10 ms to 2 ms to obtain a better temporal resolution.

Eleven curves $t_{lat}(x)$ could be obtained from the experimental data and used for further analysis. In general, all curves exhibit a similar course. The latencies increase for locations farther away from the RF center. To check whether the spatial dependence can be described by a quadratic relation as predicted by the model, the data were fitted to the function $a + bx + cx^2$, and regression coefficients were calculated. Six out of the 11 curves had a regression coefficient higher than 0.85. The remaining curves exhibited regression coefficients between 0.62 and 0.74.

Intracortical models predict a linear dependence of the firing latencies on the distance of the receptive field center (Bringuier et al., 1999). Therefore, we also fitted the data with a linear model $a + bx$. To this end, the data were split into two halves consisting of data points lying to the left and right sides of the shortest latency, respectively. One data set was vertically mirrored, and the linear fit was carried out on the resulting data, including all points.

Only in 2 of the 11 cases were regression coefficients higher than 0.85. Four cells had a coefficient between 0.62 and 0.74, and the remaining five data sets one less than 0.62.

Thus, a quadratic fit describes the experimental latency distribution better than a linear fit. This is an additional support of our hypothesis that the observed RF restructuring is caused by a thalamocortical feedforward mechanism.

Due to the nonlinear, approximately quadratic relation between x and t_{lat}, a constant speed at which the activity spreads in the cortical layer cannot be determined. Around the location of the strongest response, the instantaneous speed is higher (≈ 0.2 deg/ms) than toward the periphery (≈ 0.06 deg/ms). Averaging over the whole response area and over all subfields, an average speed of 0.1 degree per ms is obtained—for example, on average the activity travels 1 degree in 10 ms. This is comparable to literature data (Bringuier et al., 1999).

In conclusion, the results of the fit, especially the observed constant width of the potential distribution, validate the hypothesis that the restructuring from wide to small RFs can be well described by the proposed simple feedforward model and that intracortical restructuring is of only minor relevance. As explained before, a constant σ_r—a characteristic of the feedforward model—occurs only in artificial situations in feedback models.

6 Discussion

We investigated a neural field model of LGN and V1 to describe EEG-dependent RF changes in V1 (Wörgötter et al., 1998). The analytic expressions for the cortical spatiotemporal activity, equations 3.1 and 3.2, show that the restructuring can be explained by EEG-state-dependent thalamic firing patterns (burst versus tonic mode) and a pure feedforward mechanism. The restructuring is due to an "iceberg effect," with temporally fixed threshold and spatial activity profile X of constant width σ_r but a time- and state-dependent temporal profile T. This way, the region of cells above threshold, that is, the RF, varies with EEG state and over time. To test this hypothesis, the model was fitted to experimental data. Here, it is most important that the width σ_r of the spatial profiles of the estimated membrane potentials V and the firing thresholds ϑ indeed remain constant over time during a response period of 300 ms, although a strong modulation of the RF size, w, is present (as measured from spike rates). For that reason, the fit supports the hypothesis that the experimentally observed RF changes are mainly due to input from LGN and not due to recurrent synaptic interactions in V1. Models with feedback interactions lead in almost all cases to a time-dependent width σ_r. Recurrent intracortical circuits have been suggested as being responsible for the sharpening of orientation tuning curves (Ben-Yishai et al., 1995; Somers et al., 1995) but do not seem to be involved in the sharpening of spatial RF tuning.

The only parameter that showed a small systematic trend in its time course was the background activity b, which was slightly larger during the initial burst-driven part of the response (see Figure 6A). One possible reason might be that some weak excitatory connections from the LGN to a neighboring subfield exist, which are able to activate cortical cells only transiently during the strong burst component of the initial LGN response. Tanaka (1983) and Alonso and Reid (1995) investigated connections from on- or off-cells in the LGN to cortical simple cell subfields of the opposite polarity. Using cross-correlation techniques, they found that such connections are present but sparse. If the transient increase in background rates in our data is indeed due to such connections, the data indicate that those connections are not functional during the late parts of the cortical response. Consequently, their amount may be underestimated in cross-correlation studies using long-lasting stimuli.

Field models comparable to those in this article have been used to study orientation tuning of simple cells in V1 (Ben-Yishai et al., 1995; Carandini & Ringach, 1997; Somers et al., 1995). In these models the variable x just represents orientation preference of cells in a cortical column and not spatial location, as in our framework. It is a matter of discussion as to whether orientation tuning is mediated by recurrent connections inside V1 or by feedforward input from the LGN. The method presented here may help to decide that question by considering tuning widths determined from intracellular membrane potentials. Those can be measured in anesthetized cats, or—assuming a feedforward model as the null hypothesis—they can be estimated from fits of firing-rate data as in our work here. Supposing the intracellular tuning width appears to be constant in time in such experiments, the orientation tuning would likely be input driven.

Acknowledgments

K. S. and F. W. acknowledge the support of the Deutsche Forschungsgemeinschaft (SFB-509) and the HFSP. T. W. was supported in part by DFG grant Pa 268/8-1. We thank K. Funke and N. Kerscher for valuable comments and discussions and K. Funke, N. Kerscher, and Y. Zhao for help with the experimental data.

References

Adorjan, P., Levitt, J., Lund, J., & Obermayer, K. (1999). A model for the intracortical origin of orientation preference and tuning in macaque striate cortex. *Vis. Neurosci, 16*(2), 303–318.

Ahlsén, G., & Lo, F.-S. (1981). Projection of brainstem neurons to the perigeniculate nucleus and the lateral geniculate nucleus in the cat. *Brain Res., 238*, 433–438.

Alonso, R., & Reid, J.-M. (1995). Specificity of monosynaptic connections from thalamus to visual cortex. *Nature, 378*, 281–284.

Antonini, A., Gillespie, D., Crair, M., & Stryker, M. (1998). Morphology of single geniculocortical afferents and functional recovery of the visual cortex after reverse monocular deprivation in the kitten. *J. Neurosci., 18*, 9896–9909.

Ben-Yishai, R., Bar-Or, R., & Sompolinsky, H. (1995). Theory of orientation tuning in visual cortex. *Proc. Natl. Acad. Sci. USA, 92*, 3844–3848.

Bernander, Ö., Douglas, J., Martin, K., & Koch, C. (1991). Synaptic background activity influences spatiotemporal integration in single pyramidal cells. *Proc. Natl. Acad. Sci. USA, 88*, 11569–11573.

Bringuier, V., Chavane, F., Glaeser, L., & Frégnac, V. (1999). Horizontal propagation of visual activity in the synaptic integration field of area 17 neurons. *Science, 283*, 695–699.

Carandini, M., & Ringach, D. (1997). Predictions of a recurrent model of orientation selectivity. *Vis. Res., 37*, 3061–3071.

Celebrini, S., Thorpe, S., Trotter, Y., & Imbert, M. (1993). Dynamics of orientation coding in area V1 of the awake primate. *Vis. Neurosci., 10*, 811–825.

Chapman, B., Zahs, K., & Stryker, M. (1991). Relation of cortical cell orientation selectivity to alignment of receptive fields of geniculocortical afferents that arborize within a single orientation column in ferret visual cortex. *J. Neurosci, 11*, 1347–1358.

Crick, F., & Koch, C. (1998). Constraints on cortical and thalamic projections: The no-strong-loop hypothesis. *Nature, 391*, 245–250.

DeAngelis, G., Ohzawa, I., & Freeman, R. (1993). Spatiotemporal organization of simple-cell receptive fields in the cat's striate cortex. 1. General characteristics and postnatal development. *J. Neurophysiol., 69*, 1091–1117.

DeAngelis, G., Ohzawa, I., & Freeman, R. (1995). Receptive-field dynamics in the central visual pathway. *Trends Neurosci., 18*, 451–458.

Dinse, H., & Krüger, K. (1994). The timing of processing along the visual pathway in the cat. *NeuroReport, 5*, 893–897.

Eckhorn, R., Krause, F., & Nelson, J. (1993). The RF-cinematogram—a cross-correlation technique for mapping several visual receptive fields at once. *Biol. Cybern., 69*, 37–55.

Ferster, D., Chung, S., & Wheat, H. (1996). Orientation selectivity of thalamic input to simple cells of cat visual cortex. *Nature, 380*, 249–252.

Funke, K., & Eysel, U. (1998). Inverse correlation of firing patterns of single topographically matched perigeniculate neurons and cat dorsal lateral geniculate relay. *Vis. Neurosci., 15*, 711–729.

Giese, M. (1999). *Dynamic neural field theory for motion perception*. Norwell, MA: Kluwer.

Gilbert, C. (1998). Adult cortical dynamics. *Physiol. Rev., 78*, 467–485.

Henry, G., Michalski, A., Wimborne, B., & McCart, R. (1994). The nature and origin of orientation specificity in neurons of the visual pathway. *Prog. Neurobiol., 43*, 381–437.

Hirsch, J., Alonso, J.-M., Reid, R., & Martinez, L. (1998). Synaptic integration in striate cortical simple cells. *J. Neurosci, 18*, 9517–9528.

Hubel, D., & Wiesel, T. (1962). Receptive fields, binocular interaction and functional architecture in the cat's visual cortex. *J. Physiol. (London), 160*, 106–154.

Humphrey, A., Sur, M., Uhlrich, D., & Sherman, S. (1985). Projection patterns of individual x- and y-cell axons from the lateral geniculate nucleus to cortical area 17 in the cat. *J. Comp. Neurol., 233*, 159–189.

Ikeda, H., & Wright, M. (1975). Retinotopic distribution, visual latency and orientation tuning of sustained and transient cortical neurons in area 17 of the cat. *Exp. Brain Res., 22*, 385–398.

Krone, G., Mallot, H., Palm, G., & Schüz, A. (1986). Spatiotemporal receptive fields: A dynamical model derived from cortical architectonics. *Proc. R. Soc. Lond., 226*, 421–444.

Levine, M., & Shefner, J. (1991). *Fundamentals of sensation and perception* (2nd ed.). Pacific Grove, CA: Brooks/Cole.

McCormick, D. (1992). Neurotransmitter actions in the thalamus and cerebral cortex and their role in neuromodulation of thalamocortical activity. *Prog. Neurobiol., 39*, 337–388.

Mineiro, P., & Zipser, D. (1998). Analysis of direction selectivity arising from recurrent cortical interactions. *Neural Computation, 10*, 353–371.

Press, W., Teukolsky, S., Vetterling, W., & Flannery, B. (Eds.). (1993). *Numerical recipes in C: The art of scientific computing* (2nd ed.). Cambridge: Cambridge University Press.

Sabatini, S., & Solari, F. (1999). An architectural hypothesis of direction selectivity in the visual cortex: The role of spatially asymmetric intracortical inhibition. *Biol. Cybern., 80*, 171–183.

Salin, P.-A., & Bullier, J. (1995). Corticocortical connections in the visual system: Structure and function. *Physiological Rev., 75*, 107–154.

Sato, H., Katsuyama, N., Tamura, H., Hata, Y., & Tsumoto, T. (1996). Mechanisms underlying orientation selectivity of neurons in the primary visual cortex of macaque. *J. Physiol., 494*, 757–771.

Schiller, P. (1992). The on and off channels of the visual system. *TINS, 15*, 86–91.

Shevelev, I., Volgulshev, M., & Sharaev, G. (1992). Dynamics of responses of V1 neurons evoked by stimulation of different zones of the receptive field. *Neuroscience, 51*, 445–450.

Somers, D., Nelson, S., & Sur, M. (1995). An emergent model of orientation selectivity in cat visual cortical simple cells. *J. Neurosci., 15*, 5465–5488.

Sompolinsky, H., & Shapley, R. (1997). New perspectives on the mechanisms of orientation selectivity. *Current Opinion in Neurobiol., 7*, 514–522.

Tanaka, K. (1983). Cross-correlation analysis of geniculostriate neuronal relationships in cats. *J. Neurophysiol., 49*, 1303–1318.

Vidyasagar, T., Pei, X., & Vogulshev, M. (1996). Multiple mechanisms underlying the orientation selectivity of visual cortical neurones. *Trends in Neurosci., 19*, 272–277.

Wilson, H., & Cowan, J. (1973). A mathematical theory of the functional dynamics of cortical and thalamic nervous tissue. *Kybernetik, 13*, 55–80.

Wörgötter, F., & Koch, C. (1991). A detailed model of the primary visual pathway in the cat: Comparison of afferent excitatory and intracortical inhibitory connection schemes for orientation selectivity. *J. Neurosci., 11*, 1959–1979.

Wörgötter, F., Niebur, E., & Koch, C. (1991). Isotropic connections generate functional asymmetrical behavior in visual cortical cells. *J. Neurophysiol., 66*, 444–459.

Wörgötter, F., Opara, R., Funke, K., & Eysel, U. (1996). Utilizing latency for object recognition in real and artificial neural networks. *NeuroReport, 7*, 741–744.

Wörgötter, F., Suder, K., Zhao, Y., Kerscher, N., Eysel, U., & Funke, K. (1998). State-dependent receptive field restructuring in the visual cortex. *Nature, 396*, 165–168.

Received September 7, 1999; accepted April 3, 2000.